Tunable spin Hall and spin Nernst effects in Dirac line-node semimetals XCuYAs (X = Zr, Hf; Y = Si, Ge)

Babu Baijnath Prasad [1,2] and Guang-Yu Guo [1,3,*]

[1] *Department of Physics and Center for Theoretical Physics, National Taiwan University, Taipei 10617, Taiwan, Republic of China*
[2] *Nano Science and Technology Program, Taiwan International Graduate Program, Academia Sinica, Taipei 11529, Taiwan, Republic of China*
[3] *Physics Division, National Center for Theoretical Sciences, Taipei 10617, Taiwan, Republic of China*

The quaternary arsenide compounds XCuYAs (X = Zr, Hf; Y = Si, Ge) belong to the vast family of the 1111-type quaternary compounds, which possess outstanding physical properties ranging from p-type transparent semiconductors to high-temperature Fe-based superconductors. In this paper, we study the electronic structure topology, the spin Hall effect (SHE), and the spin Nernst effect (SNE) in these compounds based on density functional theory calculations. First we find that the four considered compounds are Dirac semimetals with the nonsymmorphic symmetry-protected Dirac line nodes along the Brillouin zone boundary A-M and X-R and low density of states near the Fermi level (E_F). Second, the intrinsic SHE and SNE in some of these considered compounds are found to be large. In particular, the calculated spin Hall conductivity (SHC) of HfCuGeAs is as large as -514 $(\hbar/e)$ (S/cm). The spin Nernst conductivity (SNC) of HfCuGeAs at room temperature is also large, being -0.73 $(\hbar/e)$ (A/m K). Moreover, both the magnitude and sign of the SHC and SNC in these compounds can be manipulated by varying either the applied electric field direction or the spin current direction. The SHE and SNE in these compounds can also be enhanced by tuning the Fermi level via chemical doping or electric gating. Finally, a detailed analysis of the band-decomposed and k-resolved spin Berry curvatures reveals that these large SHC and SNC as well as their notable tunabilities originate largely from the presence of a large number of spin-orbit coupling-gapped Dirac points near the Fermi level as well as the gapless Dirac line nodes, which give rise to large spin Berry curvatures. Our findings thus suggest that the four XCuYAs compounds not only provide a valuable platform for exploring the interplay between SHE, SNE, and band topology, but they also have promising applications in spintronics and spin caloritronics.

I. INTRODUCTION

In recent years, spintronics has emerged as a major field of research in condensed matter physics due to its promising applications in energy-efficient data storage and energy harvesting [1]. The key issues in spintronics are the generation, detection, and manipulation of spin current. Indeed, advanced techniques such as injection of spin current from ferromagnets to nonmagnetic materials, as well as spin pumping [2], have been recently developed, and they made the generation of spin current feasible. On the other hand, the intriguing spin Hall effect (SHE), first predicted by Dyakonov and Perel in 1971 [3], would provide a pure spin current and does not require a magnetic material or an applied magnetic field. In a nonmagnetic material under an electric field, due to the influence of the spin-orbit coupling (SOC), conduction electrons with opposite spins would acquire opposite transverse velocities, thus giving rise to a pure transverse spin current [4]. This pure spin current, generated without an applied magnetic field nor a magnetic material, is useful for the development of low-power-consumption nanoscale spintronic devices [5]. Similarly, in a nonmagnetic material, one could also get a pure spin current when a temperature gradient (∇T) instead

of an electric field E is applied, and this is known as the spin Nernst effect (SNE) [6]. The SNE thus makes thermally driven spin currents possible and leads to a new field known as spin caloritronics [7]. Pt [8] and tungsten [9] are the few well-known examples in which the SNE as well as SHE have been widely exploited in spintronic research. Clearly, other materials that exhibit large SHE and SNE would have wide applications for spintronic and spin caloritronic devices.

Recent theoretical studies indicated that 27–30 % of all nonmagnetic crystalline materials in the Inorganic Crystal Structure Database (ICSD) are topological, with roughly 12% topological insulators and 15–18 % topological semimetals [10–14]. Furthermore, recent theoretical studies on the SHE in Weyl semimetal TaAs [15] and metallic rutile oxide Dirac semimetals [16] revealed that gapped topological nodal points and lines could lead to a very large spin Hall conductivity (SHC). Also, it was recently reported that the predicted large SHE and SNE in tetragonal Dirac semimetals ZrXY (X = Si, Ge; Y = S, Se, Te) result from the presence of many slightly gapped Dirac nodal points near the Fermi level [17]. The four quaternary arsenide XCuYAs (X = Zr, Hf; Y = Si, Ge) compounds considered here have the same tetragonal symmetry (space group $P4/nmm$) as the ZrXY compounds. As for the XCuYAs compounds, they belong to the structure type of the vast family of the so-called 1111-like quaternary phases, which exhibit outstanding physical properties from
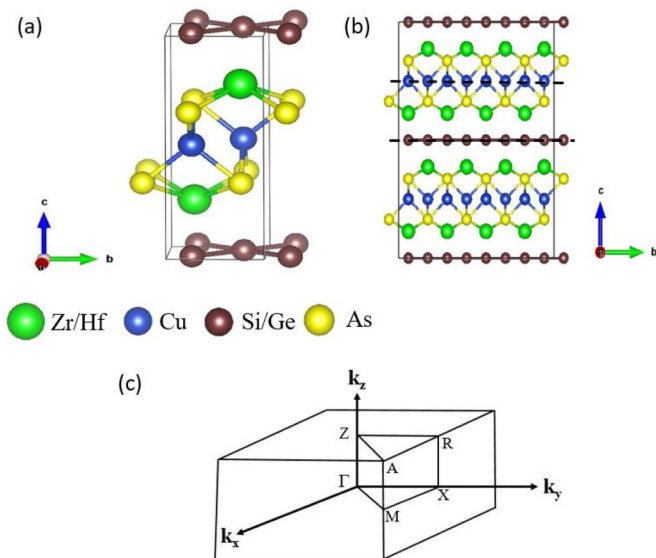
*gyguo@phys.ntu.edu.tw

FIG. 1. (a) Crystal structure of the $XCuYAs$ ($X =$ Zr, Hf; $Y =$ Si, Ge) family, (b) illustration of its nonsymmorphic glide mirror symmetry, depicting that the Cu and Si/Ge layers serve as the glide mirror planes as indicated by the black dashed lines, and (c) the corresponding tetragonal Brillouin zone (BZ).

p-type transparent semiconductors to high-temperature Fe-based superconductors. Nevertheless, only a few studies on these $XCuYAs$ compounds have been carried out so far, and these previous studies were focused mainly on the structural, elastic, and electronic properties as well as chemical bonding and stability of these quaternary arsenides [18–21]. Also, the SHE and SNE in these compounds have not been studied yet.

In this work, therefore, we systematically study the electronic structure, SHE, and SNE in the $XCuYAs$ ($X =$ Zr, Hf; $Y =$ Si, Ge) compounds by performing *ab initio* density functional theory (DFT) calculations. The rest of this paper is organized as follows. In Sec. II, we introduce the crystal

structure of the compounds, and we briefly describe the Berry phase formalism for calculating the intrinsic spin Hall and Nernst conductivities as well as the *ab initio* computational details. The main results are presented in Sec. III, which consists of four subsections. In this section, we first examine the calculated relativistic band structures and density of states of the four considered compounds in Sec. III A, which reveal the symmetry-protected Dirac line nodes as well as a large number of SOC-gapped Dirac nodal points. We then report the calculated SHC and SNC, and we also compare them with that in other well-known materials in Secs. III B and III C, respectively. In Sec. III D, in order to understand the origins of the large SHC and SNC in some of the considered compounds, we present the band-decomposed and k-resolved spin Berry curvatures for the energy bands near the Fermi level along the high-symmetry lines in the Brillouin zone. Finally, we give a summary of the conclusions drawn from this work in Sec. IV.

II. THEORY AND COMPUTATIONAL DETAILS

All four $XCuYAs$ ($X =$ Zr, Hf; $Y =$ Si, Ge) compounds belong to the tetragonal 1111-like quaternary arsenide ZrCu-SiAs family with space group $P4/nmm$. Figure 1(a) shows their crystal structure with two formula units per unit cell. Table I lists the experimental lattice constants of all four considered compounds used in the present *ab initio* study. The experimentally determined atomic positions are also used for all the compounds except HfCuGeAs. Because the experimental atomic coordinates of HfCuGeAs are not available, we determine the atomic coordinates of HfCuGeAs theoretically while keeping the lattice constants fixed to the experimental values.

Our self-consistent electronic structure calculations as well as the theoretical determination of the atomic coordinates of HfCuGeAs are based on the DFT with the generalized gradient approximation (GGA) in the form of Perdew-Burke-Ernzerhof (PBE) [22]. The accurate projector augmented-wave method [23], as implemented out in

TABLE I. Experimental lattice constants (a, c), calculated density of states at the Fermi level [$N(E_F)$] (states/eV/f.u.), spin Hall conductivity (σ_{xy}^z, σ_{xz}^y, and σ_{zx}^y), and spin Nernst conductivity (α_{xy}^z, α_{xz}^y, and α_{zx}^y) at temperature $T = 300$ K. Previous results for Dirac semimetal ZrGeTe, noncollinear antiferromagnetic Mn_3Ge, and heavy metal Pt are also listed for comparison. Note that the unit of the spin Hall conductivity (spin Nernst conductivity) is ($\hbar/e$) (S/cm) [($\hbar/e$) (A/m K)].

System	a (Å)	c (Å)	$N(E_F)$	σ_{xy}^z	σ_{xz}^y	σ_{zx}^y	α_{xy}^z	α_{xz}^y	α_{zx}^y
ZrCuSiAs	3.6736[a]	9.5712[a]	0.67	−45	−100	−175	0.20	−0.17	−0.22
ZrCuGeAs	3.7155[b]	9.5644[b]	0.56	−112	−128	−193	0.16	−0.32	−0.54
HfCuSiAs	3.6340[a]	9.6010[a]	0.65	−168	−279	−400	0.46	−0.45	−0.49
HfCuGeAs	3.6935[b]	9.5557[b]	0.57	−207	−346	−514	0.53	−0.52	−0.73
ZrGeTe[c]			1.12	136	−262	−551	0.53	0.48	1.17
Mn_3Ge[d]			2.37	56			0.14		
Pt			1.75	2139[e]			−1.09 (−0.91)[d], −1.57[f]		

[a]X-ray diffraction experiment [18].
[b]X-ray diffraction experiment [20].
[c]*Ab initio* calculation [17].
[d]*Ab initio* calculation [31].
[e]*Ab initio* calculation [28].
[f]Experiment at 255 K [8].

the Vienna Ab Initio Simulation Package (VASP) [24,25], is used. The valence electronic configurations of Zr, Hf, Cu, Si, Ge, and As taken into account in the present study are $4s^2 4p^6 4d^2 5s^2$, $5d^2 6s^2$, $3d^{10} 4s^1$, $3s^2 3p^2$, $3d^{10} 4s^2 4p^2$, and $4s^2 4p^3$, respectively. The plane-wave basis set with a large energy cutoff of 450 eV is used. In the self-consistent band structure calculations, a Γ-centered k-point mesh of $10 \times 10 \times 4$ is used in the BZ integration by the tetrahedron method [26,27]. However, a denser k-point grid of $20 \times 20 \times 8$ is used for the density of states (DOS) calculations.

The spin Hall conductivity (SHC) and spin Nernst conductivity (SNC) are calculated within the elegant Berry-phase formalism [28,29]. Within this formalism, the spin Hall conductivity ($\sigma_{ij}^s = J_i^s / E_j$) is simply given as a BZ integration of the spin Berry curvature for all the occupied bands below the Fermi level (E_F),

$$\sigma_{ij}^s = -e \sum_n \int_{BZ} \frac{d\mathbf{k}}{(2\pi)^3} f_{\mathbf{k}n} \Omega_{ij}^{n,s}(\mathbf{k}), \quad (1)$$

$$\Omega_{ij}^{n,s}(\mathbf{k}) = -\sum_{n' \neq n} \frac{2 \operatorname{Im}[\langle \mathbf{k}n | \{\tau_s, v_i\}/4 | \mathbf{k}n' \rangle \langle \mathbf{k}n' | v_j | \mathbf{k}n \rangle]}{(\epsilon_{\mathbf{k}n} - \epsilon_{\mathbf{k}n'})^2}, \quad (2)$$

where J_i^s is the ith component of the spin current density J^s, E_j is the jth component of the electric field, $f_{\mathbf{k}n}$ is the Fermi distribution function, and $\Omega_{ij}^{n,s}(\mathbf{k})$ is the spin Berry curvature for the nth band at $\mathbf{k}$, respectively, with $i, j \in (x, y, z)$ and $i \neq j$. Here, s denotes the spin direction. Also, τ_s and v_i correspond to the Pauli matrix and the velocity operator, respectively [30]. Similarly, the spin Nernst conductivity ($\alpha_{ij}^s = -J_i^s / \nabla_j T$) can be written as [29,31]

$$\alpha_{ij}^s = \frac{1}{T} \sum_n \int_{BZ} \frac{d\mathbf{k}}{(2\pi)^3} \Omega_{ij}^{n,s}(\mathbf{k})$$
$$\times [(\epsilon_{\mathbf{k}n} - \mu) f_{\mathbf{k}n} + k_B T \ln(1 + e^{-\beta(\epsilon_{\mathbf{k}n} - \mu)})], \quad (3)$$

where μ and k_B are the chemical potential and Boltzmann constant, respectively.

In the spin Hall and spin Nernst conductivities calculations, the velocity ($\langle \mathbf{k}n' | v_i | \mathbf{k}n \rangle$) and spin velocity ($\langle \mathbf{k}n | \{\tau_s, v_i\}/4 | \mathbf{k}n' \rangle$) matrix elements are obtained from the self-consistent relativistic band structures within the PAW formalism [32]. A homemade program [31,33] is used for the band summation and the Brillouin zone (BZ) integration with the tetrahedron method [27]. Very fine grids of 45 384 (for ZrCuSiAs and HfCuGeAs), 43 493 (for HfCuSiAs), and 106 272 (for ZrCuGeAs) k points in the irreducible BZ wedge are used and correspond to the division of the ΓX line into $n_d = 60$ (for ZrCuSiAs, HfCuSiAs, and HfCuGeAs) and $n_d = 80$ (for ZrCuGeAs) intervals, respectively. Test calculations using several different sets of k-point meshes show that such calculated values of the SHC and SNC for all four considered compounds converge within a few percent.

III. RESULTS AND DISCUSSION

A. Electronic structure

We first study the possible magnetic states in all four XCuYAs (X = Zr, Hf; Y = Si, Ge) compounds. We perform self-consistent spin-polarized calculations for both the ferromagnetic and antiferromagnetic states. Nevertheless, we
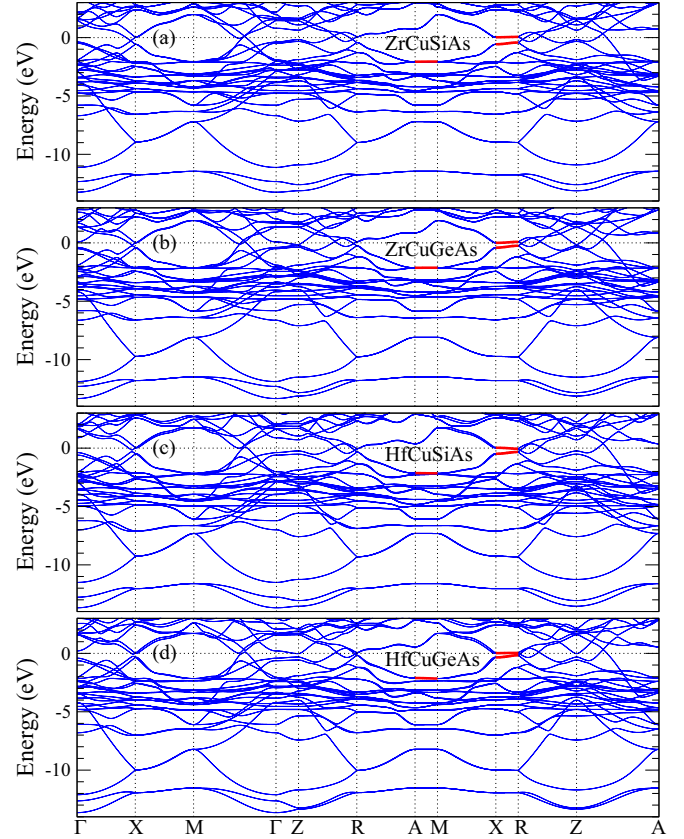
FIG. 2. Relativistic band structures of (a) ZrCuSiAs, (b) ZrCuGeAs, (c) HfCuSiAs, and (d) HfCuGeAs. In (a), (b), (c), and (d), the Fermi level is at the zero energy. The red curves represent the Dirac line nodes.

find that both magnetic states cannot be stabilized in these compounds, and this thus indicates that they are nonmagnetic. The calculated relativistic band structures and density of states (DOS) of the nonmagnetic XCuYAs (X = Zr, Hf; Y = Si, Ge) are displayed, respectively, in Figs. 2 and 3. Figure 3 shows that the lowest two valence bands of the compounds (see Fig. 2) are derived from As s-orbitals. Above these bands are the dispersive Si (Ge) sp-dominated valence bands in ZrCuSiAs and HfCuSiAs (ZrCuGeAs and HfCuGeAs) (see Figs. 2 and 3). The valence bands in between -2.0 and -6.0 eV in ZrCuSiAs and HfCuSiAs (ZrCuGeAs and HfCuGeAs) are mainly contributed from the Cu d orbitals together with small contributions from the Zr (Hf) d orbital, Si (Ge) p orbital, and As p orbital. On the other hand, the valence bands and conduction bands in the vicinity of the Fermi level (E_F) (Fig. 2) are mainly contributed from either the Zr d orbital for ZrCuSiAs and ZrCuGeAs or the Hf d orbital for HfCuSiAs and HfCuGeAs, as can be seen from the atom-decomposed DOS spectra in Fig. 3. Figure 2 also shows that all four considered compounds are semimetals with few bands crossing E_F and thus they have low DOS values near E_F (see Fig. 3).

Importantly, Fig. 2 reveals that all four considered XCuYAs compounds possess a number of slightly gapped Dirac points near E_F along the Γ-X, M-Γ, Z-R, and Z-A lines in the BZ having major contributions from the Zr (Hf)
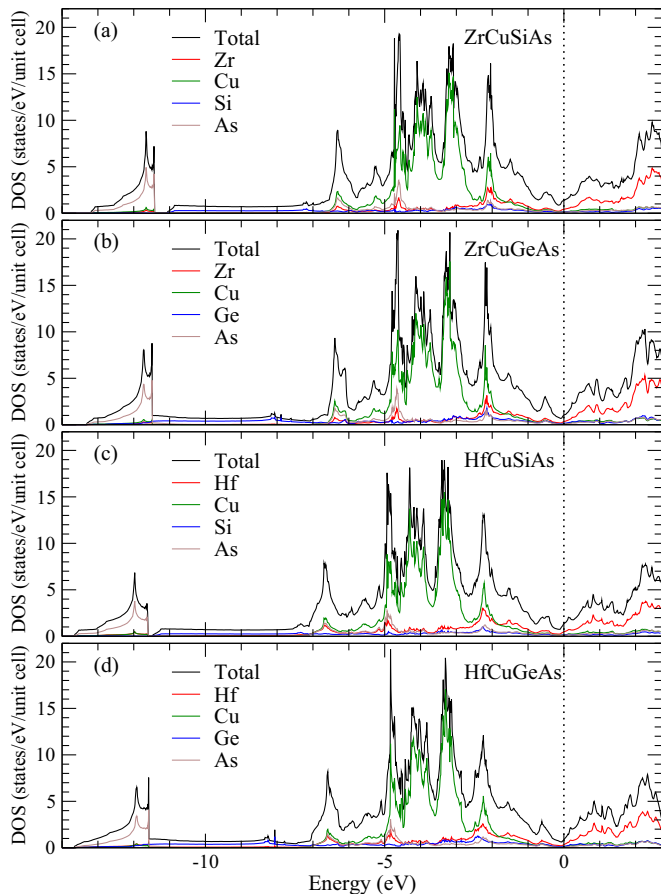
FIG. 3. Total and atom-decomposed density of states (DOS) of (a) ZrCuSiAs, (b) ZrCuGeAs, (c) HfCuSiAs, and (d) HfCuGeAs. In (a), (b), (c), and (d), the Fermi level is at the zero energy.

FIG. 4. ZrCuSiAs. (a) Relativistic band structure; (b) spin Hall conductivity (SHC; σ_{xy}^z, σ_{xz}^y, and σ_{zx}^y) as a function of energy; (c) spin Nernst conductivity (SNC; α_{xy}^z, α_{xz}^y, and α_{zx}^y) at $T = 300$ K as a function of energy; (d), (f), and (h) band-decomposed spin Berry curvatures (Ω^n); as well as (e), (g), and (i) total spin Berry curvatures (Ω) along the high-symmetry lines in the Brillouin zone. In (a), (b), and (c), the Fermi level is at zero energy, and the unit of the SHC (SNC) is ($\hbar/e$) (S/cm) [($\hbar/e$) (A/m K)]. Note that in (a), (d), (f), and (h), the same color curves correspond to the same bands.

d orbital [see also Figs. 4(a), 5(a), 6(a), and 7(a) below]. In contrast, in the scalar-relativistic band structures (i.e., without SOC) (not shown here), these Dirac points are gapless, which is a general feature of the layered tetragonal systems of type ZrSiS(Se), and they are protected by C_{2v} symmetry along those lines. In the presence of SOC, however, the number of irreducible representations of the C_{2v} point group is reduced to 1, and consequently these Dirac points are gapped out. As will be shown in Sec. III D, these gapped Dirac points exhibit large spin Berry curvatures and thus make significant contributions to the SHC and SNC [see Eqs. (1) and (3)]. Interestingly, we also find that there are Dirac line nodes along the *A-M* and *X-R* on the BZ boundary (see the red curves in Fig. 2), similar to that of the ZrXY family [17]. These Dirac line nodes are protected by the nonsymmorphic glide mirror symmetry where Cu and Si/Ge layers serve as the glide mirror planes for the glide operation ($M_c | \frac{1}{2} \frac{1}{2} 0$), as shown in Fig. 1(b) with black dashed lines. Therefore, they are not gapped out in the presence of the SOC. The Dirac line nodes along the *A-M* are 2.0 eV below E_F and thus would not significantly influence the transport properties such as SHC and SNC. In contrast, the Dirac line nodes along the *X-R* are close to the Fermi level and thus will have significant effects on the transport properties of these compounds.
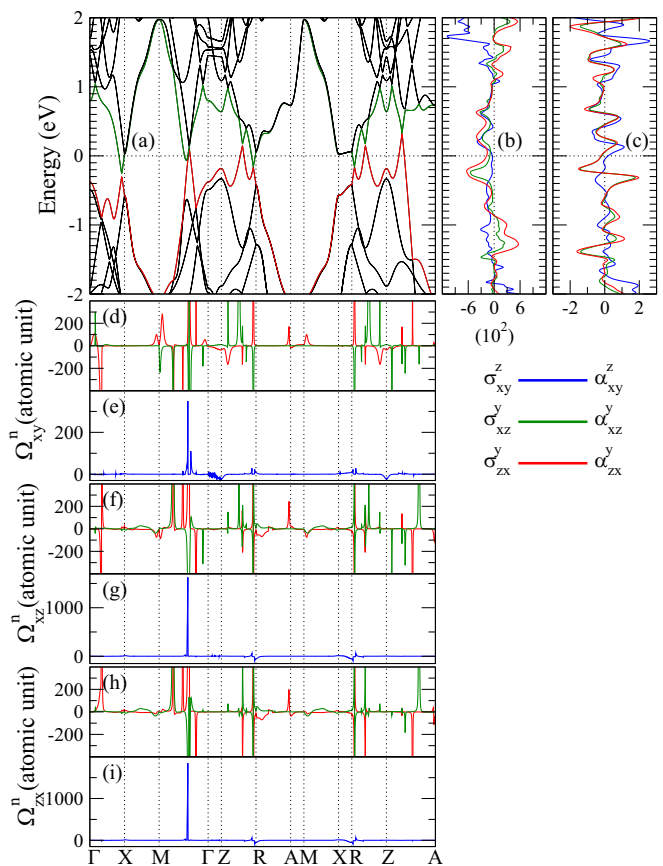
B. Spin Hall effect

The SHC of a solid is a third-rank tensor (σ_{ij}^s; $s, i, j = x, y, z$). Nevertheless, only a few of the elements of the SHC tensor are nonvanishing because of the symmetry constraints. For the nonmagnetic XCuYAs (X = Zr, Hf; Y = Si, Ge) compounds having space group $P4/nmm$, as revealed by a recent symmetry analysis [34], there are only five nonzero tensor elements. Also note that because of the tetragonal symmetry of these compounds, the x and y axes are equivalent, and this results in $\sigma_{yz}^x = -\sigma_{xz}^y$ and $\sigma_{zx}^y = -\sigma_{zy}^x$. Therefore, we end up with only three independent nonzero elements, namely σ_{xy}^z, σ_{xz}^y, and σ_{zx}^y, where superscripts x, y, and z denote, respectively, the spin direction of the spin current along the [100], [010], and [001] directions, as listed in Table II. The calculated values of all the nonzero SHC tensor elements for the XCuYAs family are listed in Table I. In Table I, σ_{xy}^z, σ_{xz}^y, and σ_{zx}^y of a recently studied Dirac semimetal ZrGeTe [17], as well as σ_{xy}^z of noncollinear antiferromagnet Mn$_3$Ge [31] and platinum metal [8,28], are also listed for comparison.
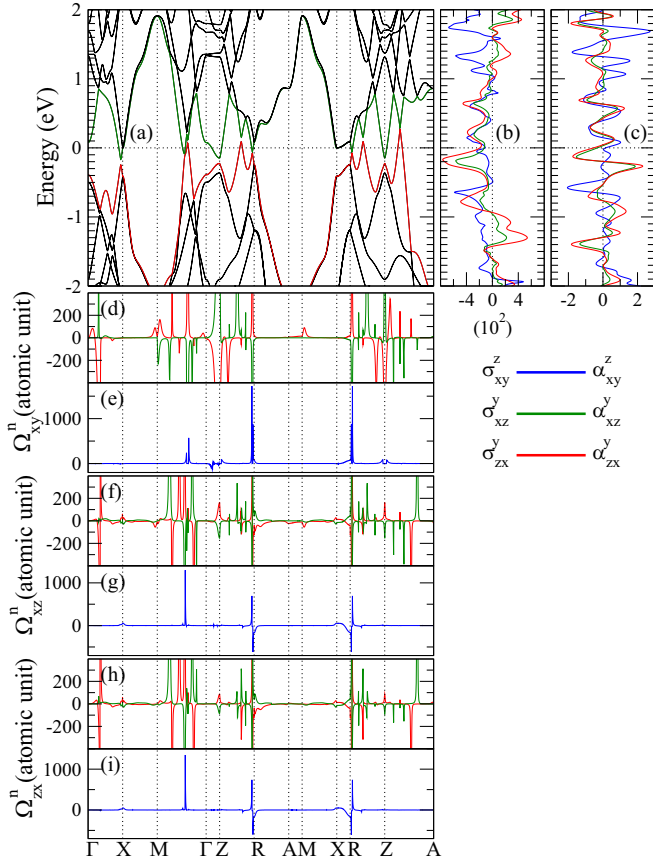
FIG. 5. ZrCuGeAs. (a) Relativistic band structure; (b) spin Hall conductivity (SHC; σ_{xy}^{z}, σ_{xz}^{y}, and σ_{zx}^{y}) as a function of energy; (c) spin Nernst conductivity (SNC; α_{xy}^{z}, α_{xz}^{y}, and α_{zx}^{y}) at $T = 300$ K as a function of energy; (d), (f), and (h) band-decomposed spin Berry curvatures (Ω^{n}); as well as (e), (g), and (i) total spin Berry curvatures (Ω) along the high-symmetry lines in the Brillouin zone. In (a), (b), and (c), the Fermi level is at zero energy, and the unit of the SHC (SNC) is $(\hbar/e)$ (S/cm) [$(\hbar/e)$ (A/m K)]. Note that in (a), (d), (f), and (h), the same color curves correspond to the same bands.

FIG. 6. HfCuSiAs. (a) Relativistic band structure; (b) spin Hall conductivity (SHC; σ_{xy}^{z}, σ_{xz}^{y}, and σ_{zx}^{y}) as a function of energy; (c) spin Nernst conductivity (SNC; α_{xy}^{z}, α_{xz}^{y}, and α_{zx}^{y}) at $T = 300$ K as a function of energy; (d), (f), and (h) band-decomposed spin Berry curvatures (Ω^{n}); as well as (e), (g), and (i) total spin Berry curvatures (Ω) along the high-symmetry lines in the Brillouin zone. In (a), (b), and (c), the Fermi level is at zero energy, and the unit of the SHC (SNC) is $(\hbar/e)$ (S/cm) [$(\hbar/e)$ (A/m K)]. Note that in (a), (d), (f), and (h), the same color curves correspond to the same bands.

In Table I, we list the results for the four XCuYAs compounds in the increasing order of their SOC strength. It is clear from Table I that all the nonzero SHC elements, i.e., σ_{xy}^{z}, σ_{xz}^{y}, and σ_{zx}^{y}, increase monotonically as we go down from ZrCuSiAs to HfCuGeAs, and this is consistent with the SOC strength among these materials. The calculated value of σ_{zx}^{y} for HfCuGeAs is the largest, being -514 $(\hbar/e)$ (S/cm) and about four times smaller than the SHC (σ_{xy}^{z}) [2139 $(\hbar/e)$ (S/cm)] of platinum metal, which has the largest intrinsic SHC among the transition metals [28,33]. Interestingly, σ_{zx}^{y} for HfCuGeAs is nine times larger than that [56 $(\hbar/e)$ (S/cm)] of the non-collinear antiferromagnet Mn$_3$Ge [31] and is comparable to the calculated value of σ_{zx}^{y} of ZrGeTe, which has the largest SOC strength among the ZrXY family [17]. Also, σ_{zx}^{y} of HfCuSiAs [-400 $(\hbar/e)$ (S/cm)] is 1.5 times larger than that [-262 $(\hbar/e)$ (S/cm)] of σ_{zx}^{y} of ZrGeTe [17].

There is a strong anisotropy in the SHC in the XCuYAs compounds, as displayed in Table I. For example, the SHC value of ZrCuSiAs can be increased by a factor of 4 by ch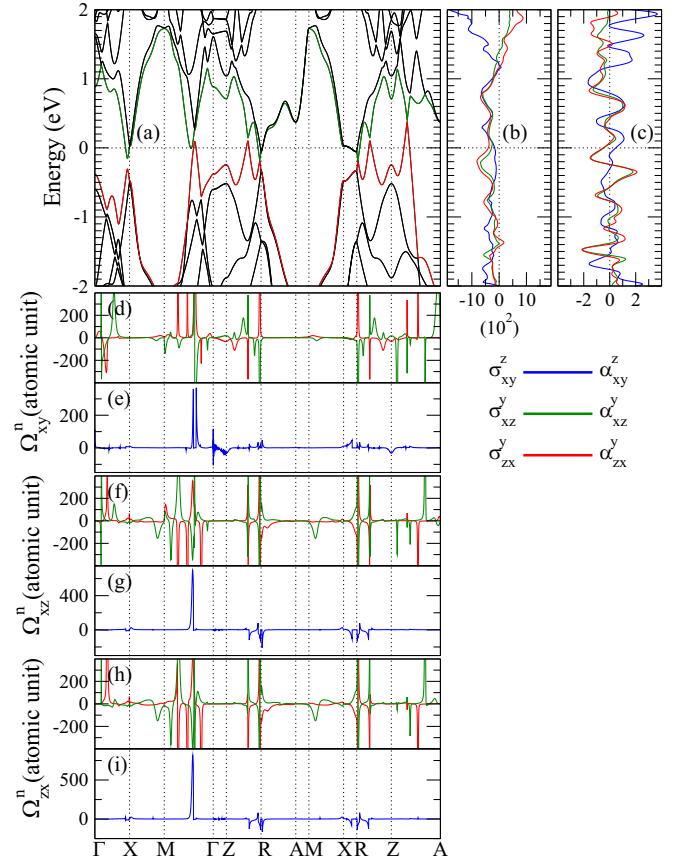anging the spin polarization of the spin current from the z (out-of-plane) direction to either the x or y (in-plane) direction. Also, for HfCuSiAs and HfCuGeAs, the SHC can be increased by a factor of approximately 2.4 and 2.5, respectively, when the spin polarization is switched from the z to either the x or y direction. The calculated SHC for the XCuYAs compounds also depends strongly on the direction of the applied electric field, as can be seen from Table I. For all four compounds, the SHC value for the electric field applied along the [100] direction (σ_{zx}^{y}) is approximately 1.5 times larger than that along the [001] direction (σ_{xz}^{y}; see Table I).

We have also calculated the SHC as a function of Fermi energy (E_F) within the rigid-band approximation in which only the Fermi energy is varied while keeping the band structure fixed. The calculated SHC spectra are presented in Figs. 4(b), 5(b), 6(b), and 7(b) for ZrCuSiAs, ZrCuGeAs, HfCuSiAs, and HfCuGeAs, respectively. It is clear that most of the nonzero elements of the SHC tensor have peaks in the vicinity of the Fermi energy, suggesting that the SHE in these compounds can be optimized by varying E_F via either chemical doping or electrical gating. For example, σ_{xy}^{z} of ZrCuGeAs can be
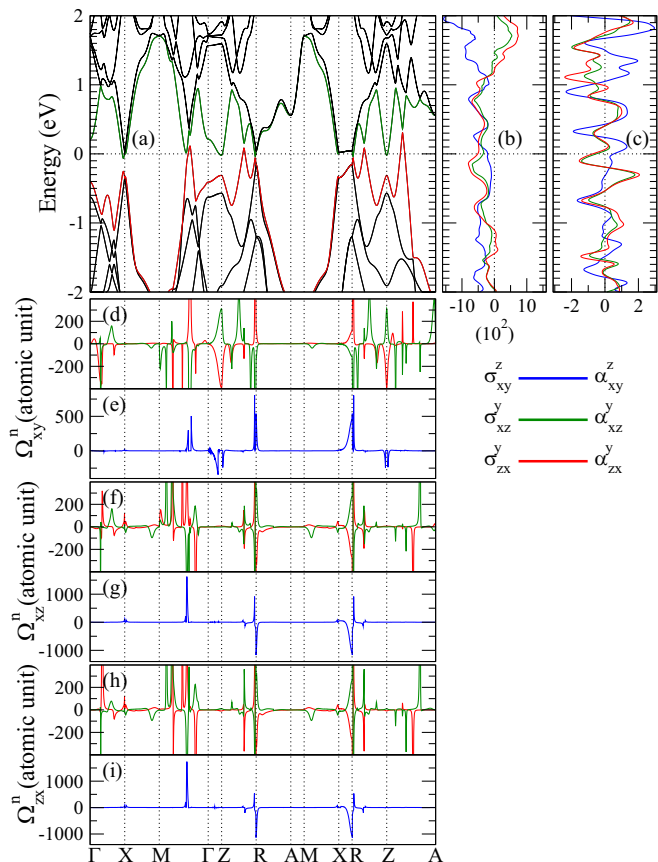
FIG. 7. HfCuGeAs. (a) Relativistic band structure; (b) spin Hall conductivity (SHC; σ_{xy}^z, σ_{xz}^y, and σ_{zx}^y) as a function of energy; (c) spin Nernst conductivity (SNC; α_{xy}^z, α_{xz}^y, and α_{zx}^y) at $T = 300$ K as a function of energy; (d), (f), and (h) band-decomposed spin Berry curvatures (Ω^n); as well as (e), (g), and (i) total spin Berry curvatures (Ω) along the high-symmetry lines in the Brillouin zone. In (a), (b), and (c), the Fermi level is at zero energy, and the unit of the SHC (SNC) is $(\hbar/e)$ (S/cm) $[(\hbar/e)$ (A/m K)]. Note that in (a), (d), (f), and (h), the same color curves correspond to the same bands.

increased by a factor of 2 by slightly lowering the Fermi energy by 0.05 eV [see Fig. 5(b)]. This can be achieved by hole doping of merely 0.03 e/f.u. Also, σ_{zx}^y of HfCuGeAs could be enhanced from -514 $(\hbar/e)$ (S/cm) to -801 $(\hbar/e)$ (S/cm) by lowering the Fermi energy to -0.14 eV [see Fig. 7(b)], and this can be realized via hole doping of 0.07 e/f.u.

C. Spin Nernst effect

Similar to the SHC for a solid, SNC (α_{ij}^s; $s, i, j = x, y, z$) is also a third-rank tensor. Furthermore, the nonzero elements of the SNC tensor are identical to that of the SHC tensor [34]. Therefore, for the XCuYAs (X = Zr, Hf; Y = Si, Ge) compounds, the SNC has only three nonzero independent tensor elements, namely α_{xy}^z, α_{xz}^y, and α_{zx}^y. We list the calculated values of these nonzero SNC elements at $T = 300$ K in the XCuYAs family in Table I. We notice that α_{zx}^y of HfCuGeAs is the largest [-0.73 $(\hbar/e)$ (A/m K)] among the XCuYAs family. Also, it is almost five times larger than α_{xy}^z [0.14 $(\hbar/e)$ (A/m K)] of the noncollinear antiferromagnet Mn$_3$Ge [31]. The α_{xy}^z values of HfCuGeAs and ZrGeTe [17] are equal.

	SHC		
$\underline{\sigma}^x$		$\underline{\sigma}^y$	$\underline{\sigma}^z$
$\begin{pmatrix} 0 & 0 & 0 \\ 0 & 0 & -\sigma_{xz}^y \\ 0 & -\sigma_{zx}^y & 0 \end{pmatrix}$		$\begin{pmatrix} 0 & 0 & \sigma_{xz}^y \\ 0 & 0 & 0 \\ \sigma_{zx}^y & 0 & 0 \end{pmatrix}$	$\begin{pmatrix} 0 & \sigma_{xy}^z & 0 \\ -\sigma_{xy}^z & 0 & 0 \\ 0 & 0 & 0 \end{pmatrix}$

They are comparable to that of Pt metal, being about half the α_{xy}^z value of Pt (Table I). Therefore, we can say that the SNC values for the XCuYAs compounds are significant.

The SNC of the four XCuYAs compounds is also highly anisotropic, similar to the SHC. For example, the α_{zx}^y of Zr-CuGeAs is approximately 3.4 times larger than α_{xy}^z of the same material (see Table I), i.e., the SNC value of ZrCuGeAs is enhanced by a factor of 3.4 when the spin direction of the spin current is switched from the z to the x or y direction. Unlike the SHC, the SNC of the XCuYAs family changes sign when the spin direction of the spin current is rotated from the out-of-plane (z) direction to an in-plane (x or y) direction. For HfCuGeAs, α_{zx}^y is 1.4 times larger than α_{xz}^y (see Table I).

The SNC at $T = 300$ K has also been calculated as a function of E_F and is displayed in Figs. 4(c), 5(c), 6(c), and 7(c), respectively, for ZrCuSiAs, ZrCuGeAs, HfCuSiAs, and HfCuGeAs. These SNC spectra will allow one to optimize the SNE in the XCuYAs compounds via manipulation of E_F. For example, Fig. 5(c) indicates that the α_{xy}^z of ZrCuGeAs has a prominent peak of 1.02 $(\hbar/e)$ (A/m K) at 0.08 eV (just slightly above E_F). This suggests that the SNC α_{xy}^z of ZrCuGeAs can be substantially increased from 0.16 to 1.02 $(\hbar/e)$ (A/m K) via electron doping of merely 0.05 e/f.u. Note that this value of α_{xy}^z is very close to that of platinum metal [-1.09 $(\hbar/e)$ (A/m K)] [31], thus indicating the possible application of these materials in spin caloritronic devices. The α_{zx}^y of HfCuGeAs also has a peak of -1.53 $(\hbar/e)$ (A/m K) at -0.10 eV (slightly below E_F), and this could be achieved by hole doping of merely 0.06 e/f.u. [see Fig. 7(c)]. The SNC spectra of the XCuYAs family display a stronger dependence on E_F than that of the SHC. For example, α_{zx}^y of ZrCuSiAs decreases rapidly as E_F decreases and then reaches the negative local maximum of -1.51 $(\hbar/e)$ (A/m K) at -0.19 eV. As we decrease E_F further, it increases steadily and changes sign at -0.25 eV and then hits the positive local maximum of 1.96 $(\hbar/e)$ (A/m K) at -0.32 eV [see Fig. 4(c)]. For ZrCuGeAs, α_{zx}^y decreases as E_F decreases and reaches a negative local maximum of -1.74 $(\hbar/e)$ (A/m K) at -0.12 eV. It starts to increase as E_F is lowered further, changes sign at -0.19 eV, and then rises to a positive local maximum of 2.30 $(\hbar/e)$ (A/m K) at -0.26 eV [see Fig. 5(c)]. The α_{xy}^z for the four XCuYAs compounds shows a similar behavior [see Figs. 4(c)–7(c)]. All these suggest that electric gating or chemical doping can be used to manipulate the SHE and SNE in the XCuYAs compounds.

The temperature (T) dependence of the SNC of all four XCuYAs compounds is also calculated in the present study.
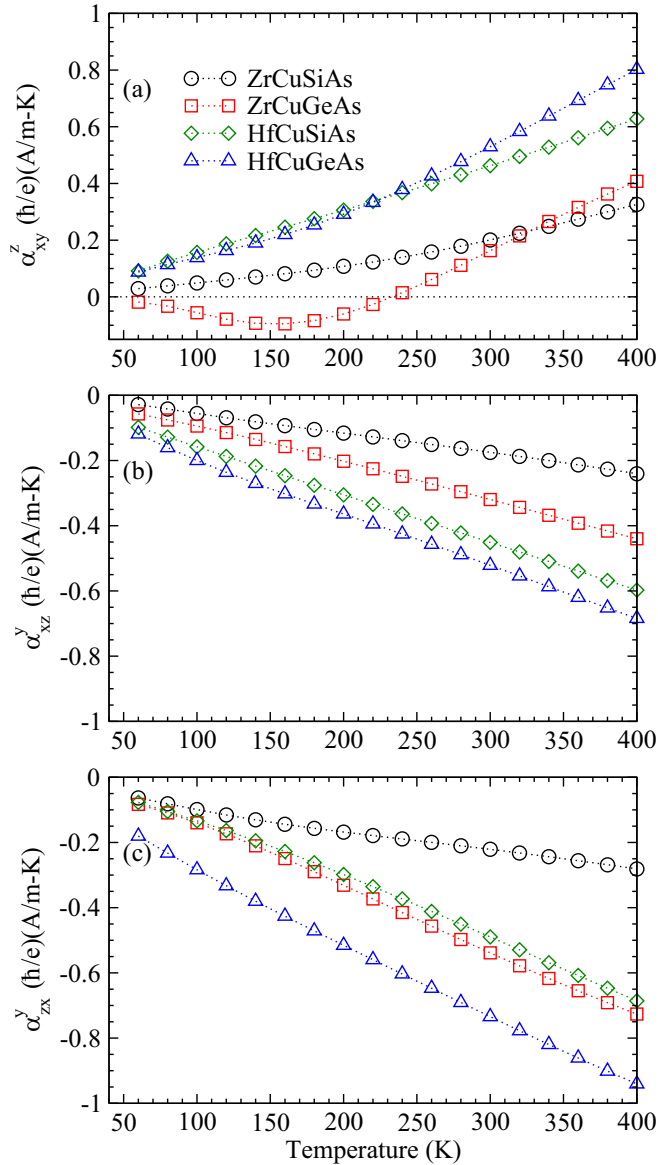
FIG. 8. Spin Nernst conductivity (a) α_{xy}^z, (b) α_{xz}^y, and (c) α_{zx}^y as a function of temperature T for the four XCuYAs compounds.

Figure 8 shows the calculated T dependences of α_{xy}^z, α_{xz}^y, and α_{zx}^y. We notice that both α_{xz}^y and α_{zx}^y for all four compounds are negative, and their magnitudes increase monotonically as T increases from $T = 60$ to 400 K [see Figs. 8(b) and 8(c)]. Also, HfCuGeAs has the largest magnitude of α_{xz}^y and α_{zx}^y among the four compounds in the entire considered T range. The values of α_{xz}^y and α_{zx}^y for HfCuGeAs hit the negative maximum of -0.68 and -0.94 ($\hbar/e$) (A/m K), respectively, at $T = 400$ K (see Fig. 8). Interestingly, the α_{zx}^y spectra of ZrCuGeAs and HfCuSiAs have almost an identical behavior, and their calculated values are close in the entire considered temperature range. In contrast, the α_{xy}^z spectra of ZrCuSiAs, HfCuSiAs, and HfCuGeAs have a positive value, and all of them increase monotonically with T [see Fig. 8(a)]. Interestingly, the values of α_{xy}^z for HfCuSiAs and HfCuGeAs are nearly identical for $T \leqslant 260$ K. However, α_{xy}^z of ZrCuGeAs

has a negative value at $T = 60$ K. It decreases monotonically with T and reaches the negative local maximum of -0.095 ($\hbar/e$) (A/m K) at $T = 160$ K. As temperature T further increases, it starts to increase, then changes sign at $\sim$240 K, and finally reaches the maximum value of 0.41 ($\hbar/e$) (A/m K) at $T = 400$ K [see Fig. 8(a)].

D. Spin Berry curvature analysis

Spin Berry curvature is the key ingredient for calculating spin Hall and spin Nernst conductivities, as can be seen from Eqs. (1) and (3), respectively. Thus, in order to understand the origin of the SHC and SNC for the XCuYAs compounds, we have calculated total and band-decomposed spin Berry curvatures for the energy bands near the Fermi level as a function of the k-point. The total spin Berry curvature at **k** is the sum of the spin Berry curvatures of all the occupied bands at **k**. Figures 4(d), 4(f) and 4(h); Figs. 5(d), 5(f) and 5(h); Figs. 6(d), 6(f) and 6(h); and Figs. 7(d), 7(f) and 7(h) show these spin Berry curvatures Ω_{xy}^z, Ω_{xz}^y, and Ω_{zx}^y, respectively, along the high-symmetry lines in the BZ.

As mentioned before, in the XCuYAs compounds, a number of SOC-gapped Dirac points are present near the Fermi level along the Γ-X, M-Γ, Z-R, and Z-A directions in the BZ [see Fig. 2 as well as Figs. 4(a)–7(a)]. As reported previously in the literature [17,28], when a band-crossing point (e.g., a Dirac point) at **k** is slightly gapped by the SOC, a pair of spin Berry curvature peaks with opposite signs appear in the vicinity of the k point on the lower and upper gapped bands, respectively. These phenomena can be clearly seen in Figs. 4(d), 4(f) and 4(h); Figs. 5(d), 5(f) and 5(h); Figs. 6(d), 6(f) and 6(h); and Figs. 7(d), 7(f) and 7(h). Clearly, a large contribution to the SHC may occur when only the lower band is occupied. If both bands are occupied, the two peaks with opposite signs would cancel each other, thus leading to little contribution to the SHC [17].

Table I shows that HfCuGeAs has the largest values of the nonzero elements of the SHC tensor. Therefore, as an example, let us take a closer look at the energy bands near the Fermi level and their spin Berry curvatures in HfCuGeAs. First we notice that for total spin Berry curvature Ω_{xy}^z, there are sharp positive peaks at the R point as well as near the middle of the M-Γ line [see the blue curve in Fig. 7(e)]. In the meantime, we can see from Fig. 7(a) that there are gapped Dirac points at these k-points, which generate two pairs of sharp Ω_{xy}^n peaks with opposite signs at the same k-points [see the red and green curves in Fig. 7(d)]. Since only the lower band (red curve) of the gapped Dirac point is occupied [see Fig. 7(a)], the large positive Ω_{xy}^n peaks [see the red curve in Fig. 7(d)] thus give rise to the dominant contribution to the total spin Berry curvature peaks at these k-points [see Fig. 7(e)]. Similar situations happen to Ω_{xz}^n and Ω_{zx}^n near the middle of the M-Γ line [see Figs. 7(f) and 7(g) as well as Figs. 7(h) and 7(i), respectively]. Figure 5 indicates that the calculated total and band-decomposed spin Berry curvatures in ZrCuGeAs exhibit almost the same behavior as that of HfCuGeAs, although the peak magnitudes may differ. However, for ZrCuSiAs, there are only sharp positive peaks for the total spin Berry curvatures Ω_{xy}^z, Ω_{xz}^y, and Ω_{zx}^y near the middle of the M-Γ line [see the blue curves in Figs. 4(e), 4(g), and
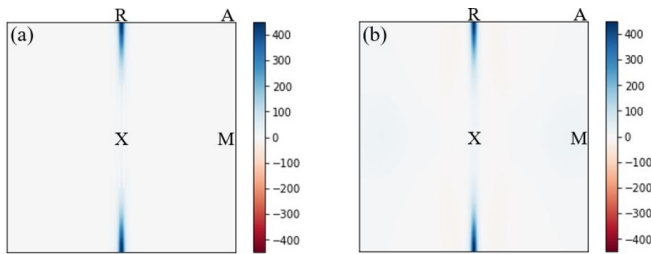
FIG. 9. Contour plot of (a) total and (b) Dirac line node only contributions to spin Berry curvature $\Omega_{xy}(\mathbf{k})$ of HfCuGeAs on the X-R-A-M plane [see Fig. 1(c)].

4(i)]. There is no other prominent peak for the total spin Berry curvatures for ZrCuSiAs except the one along the M-Γ line [see the blue curves in Figs. 4(e), 4(g), and 4(i)].

In addition to the known resonance-like contributions from the slightly gapped Dirac points, we find that the Dirac line nodes can also make a significant contribution to the total spin Berry curvature and hence to SHC as well as SNC. For example, as mentioned above, there is a Dirac line node along the X-R line slightly below the Fermi level in HfCuGeAs [see the red curve in Fig. 7(a)]. This line node generates large spin Berry curvatures Ω_{xy}^{z}, Ω_{xz}^{y}, and Ω_{zx}^{y} along this X-R line [see the red curve in Figs. 7(d), 7(f), and 7(h), respectively], thus leading to the pronounced peaks in the corresponding total spin Berry curvatures on this line near the R point [see the blue curve in Figs. 7(e), 7(g), and 7(i), respectively]. The contour plots of the total and Dirac line-node spin Berry curvatures of $\Omega_{xy}(\mathbf{k})$ on the X-R-A-M plane in the BZ in HfCuGeAs are displayed in Figs. 9(a) and 9(b), respectively. Figure 9 shows clearly that the total and Dirac line-node spin Berry curvatures $\Omega_{xy}(\mathbf{k})$ of HfCuGeAs have large values only along the X-R line. Moreover, the total spin Berry curvature comes predominantly from the Dirac line-node spin Berry curvature. Therefore, this demonstrates that the occupied Dirac line

nodes near the Fermi level can also contribute significantly to the large SHE and SNE in this Dirac line-node semimetal.

IV. CONCLUSIONS

In conclusion, we have carried out a systematic *ab initio* study on the band structure topology, SHE, and SNE in the quaternary arsenide XCuYAs ($X = $ Zr, Hf; $Y = $ Si, Ge) compounds based on relativistic density functional theory calculations. Interestingly, we find that the four considered compounds are Dirac semimetals with the nonsymmorphic symmetry-protected Dirac line nodes along the Brillouin zone boundary A-M and X-R. Furthermore, we also find that the intrinsic SHE and SNE in some of these considered compounds are large. In particular, the calculated spin Hall conductivity (SHC) of HfCuGeAs is as large as $-514\,(\hbar/e)$ (S/cm). The spin Nernst conductivity (SNC) of HfCuGeAs at room temperature is also large, being $-0.73\,(\hbar/e)$ (A/m K). Both the magnitude and sign of the SHC and SNC in these compounds are found to be tunable by varying either the applied electric field direction or the spin current direction. The SHE and SNE in these compounds can also be significantly enhanced by tuning the Fermi level via chemical doping or electric gating. We have also calculated the band-decomposed and k-resolved spin Berry curvatures, which reveal that these large SHC and SNC as well as their notable tunabilities originate largely from the presence of a large number of spin-orbit coupling-gapped Dirac points near the Fermi level as well as the gapless Dirac line nodes, which give rise to large spin Berry curvatures. Our work thus shows that the four XCuYAs compounds not only provide a valuable platform for exploring the interplay between SHE, SNE, and band topology but also have promising applications in spintronics and spin caloritronics.

[1] J. Puebla, J. Kim, K. Kondou, and Y. Otani, Spintronic devices for energy-efficient data storage and energy harvesting, Commun. Mater. **1**, 24 (2020).

[2] M. Switkes, C. Marcus, K. Campman, and A. Gossard, An adiabatic quantum electron pump, Science **283**, 1905 (1999).

[3] M. I. D'yakonov and V. I. Perel, Spin orientation of electrons associated with the interband absorption of light in semiconductors, Sov. Phys. JETP **33**, 1053 (1971).

[4] S. Murakami, N. Nagaosa, and S.-C. Zhang, Dissipationless quantum spin current at room temperature, Science **301**, 1348 (2003).

[5] L. Liu, C.-F. Pai, Y. Li, H.-W. Tseng, D. C. Ralph, and R. A. Buhrman, Spin-torque switching with the giant spin Hall effect of tantalum, Science **336**, 555 (2012).

[6] S. Cheng, Y. Xing, Q.-F. Sun, and X. C. Xie, Spin Nernst effect and Nernst effect in two-dimensional electron systems, Phys. Rev. B **78**, 045302 (2008).

[7] G. E. W. Bauer, E. Saitoh, and B. J. van Wees, Spin caloritronics, Nat. Mater. **11**, 391 (2012).

[8] S. Meyer, Y.-T. Chen, S. Wimmer, M. Althammer, T. Wimmer, R. Schlitz, S. Geprägs, H. Huebl, D. Ködderitzsch, H. Ebert, G. E. W. Bauer, R. Gross, and S. T. B. Goennenwein, Observation of the spin Nernst effect, Nat. Mater. **16**, 977 (2017).

[9] P. Sheng, Y. Sakuraba, Y.-C. Lau, S. Takahashi, S. Mitani, and M. Hayashi, The spin Nernst effect in tungsten, Sci. Adv. **3**, e1701503 (2017).

[10] F. Tang, H. C. Po, A. Vishwanath, and X. Wan, Efficient topological materials discovery using symmetry indicators, Nat. Phys. **15**, 470 (2019).

[11] T. Zhang, Y. Jiang, Z. Song, H. Huang, Y. He, Z. Fang, H. Weng, and C. Fang, Catalogue of topological electronic materials, Nature (London) **566**, 475 (2019).

[12] M. G. Vergniory, L. Elcoro, C. Felser, N. Regnault, B. A. Bernevig, and Z. Wang, A complete catalog of high-quality topological materials, Nature (London) **566**, 480 (2019).

[13] F. Tang, H. C. Po, A. Vishwanath, and X. Wan, Comprehensive search for topological materials using symmetry indicators, Nature (London) **566**, 486 (2019).

[14] É. L.- Hurtubise and M. Franz, Topology in abundance, Nat. Rev. Phys. **1**, 183 (2019).

[15] Y. Sun, Y. Zhang, C. Felser, and B. Yan, Strong Intrinsic Spin Hall Effect in the TaAs Family of Weyl Semimetals, Phys. Rev. Lett. **117**, 146403 (2016).

[16] Y. Sun, Y. Zhang, C.-X. Liu, C. Felser, and B. Yan, Dirac nodal lines and induced spin Hall effect in metallic rutile oxides, Phys. Rev. B **95**, 235104 (2017).

[17] Y. Yen and G.-Y. Guo, Tunable large spin Hall and spin Nernst effects in the Dirac semimetals $ZrXY$ ($X =$ Si, Ge; $Y =$ S, Se, Te), Phys. Rev. B **101**, 064430 (2020).

[18] V. Johnson and W. Jeitschko, ZrCuSiAs: A "filled" PbFCl type, J. Solid State Chem. **11**, 161 (1974).

[19] P. E. R. Blanchard, R. G. Cavell, and A. Mar, Electronic structure of ZrCuSiAs and ZrCuSiP by X-ray photoelectron and absorption spectroscopy, J. Solid State Chem. **183**, 1536 (2010).

[20] A. M. Baergen, P. E. R. Blanchard, S. S. Stoyko, and A. Mar, Quaternary germanide arsenides ZrCuGeAs and HfCuGeAs, Z. Anorg. Allg. Chem. **637**, 2007 (2011).

[21] V. V. Bannikov, I. R. Shein, and A. L. Ivanovskii, Structural, elastic, electronic properties and stability trends of 1111-like silicide arsenides and germanide arsenides MCuXAs (M = Ti, Zr, Hf; X = Si, Ge) from first principles, J. Alloys Compd. **533**, 71 (2012).

[22] J. P. Perdew, K. Burke, and M. Ernzerhof, Generalized Gradient Approximation Made Simple, Phys. Rev. Lett. **77**, 3865 (1996).

[23] P. E. Blöchl, Projector augmented-wave method, Phys. Rev. B **50**, 17953 (1994).

[24] G. Kresse and J. Hafner, *Ab initio* molecular dynamics for liquid metals, Phys. Rev. B **47**, 558 (1993).

[25] G. Kresse and J. Furthmüller, Efficient iterative schemes for *ab initio* total-energy calculations using a plane-wave basis set, Phys. Rev. B **54**, 11169 (1996).

[26] O. Jepson and O. Anderson, The electronic structure of h.c.p. ytterbium, Solid State Commun. **9**, 1763 (1971).

[27] W. M. Termmerman, P. A. Sterne, G. Y. Guo, and Z. Szotek, Electronic structure calculations of high Tc materials, Mol. Simul. **4**, 153 (1989).

[28] G. Y. Guo, S. Murakami, T.-W. Chen, and N. Nagaosa, Intrinsic Spin Hall Effect in Platinum: First-Principles Calculations, Phys. Rev. Lett. **100**, 096401 (2008).

[29] D. Xiao, M.-C. Chang, and Q. Niu, Berry phase effects on electronic properties, Rev. Mod. Phys. **82**, 1959 (2010).

[30] G. Y. Guo, Y. Yao, and Q. Niu, *Ab initio* Calculation of the Intrinsic Spin Hall Effect in Semiconductors, Phys. Rev. Lett. **94**, 226601 (2005).

[31] G.-Y. Guo and T.-C. Wang, Large anomalous Nernst and spin Nernst effects in the noncollinear antiferromagnets Mn_3X ($X =$ Sn, Ge, Ga), Phys. Rev. B **96**, 224415 (2017); **100**, 169907(E) (2019).

[32] B. Adolph, J. Furthmüller, and F. Beckstedt, Optical properties of semiconductors using projector-augmented waves, Phys. Rev. B **63**, 125108 (2001).

[33] G. Y. Guo, Q. Niu, and N. Nagaosa, Anomalous Nernst and Hall effects in magnetized platinum and palladium, Phys. Rev. B **89**, 214406 (2014).

[34] M. Seemann, D. Kodderitzsch, S. Wimmer, and H. Ebert, Symmetry-imposed shape of linear response tensors, Phys. Rev. B **92**, 155138 (2015).